Electronic Supplementary Information (ESI)

Nickel Based Oxides Film Formed in Molten Salts for Efficient Electrocatalytic Oxygen Evolution

Xin Xin Liang, [a] Wei Weng, [a] Dong Gu [b] and Wei Xiao [*a]

a. School of Resource and Environmental Sciences, Hubei International Scientific and Technological Cooperation Base of Sustainable Resource and Energy, Wuhan University, Wuhan 430072, PR China.
b. The Institute for Advanced Studies, Wuhan University, Wuhan, Hubei 430072, P. R. China

[*]Email: gabrielxiao@whu.edu.cn; Homepage: http://wxiao.whu.edu.cn/; Tel./Fax: +86-27-68775799

Calculation Section

ECSA is usually used to reflect the activity of the electrocatalysts, which can be evaluated by the electrode/electrolyte interface double-layer capacitance (C_{dl}) and the corresponding roughness factors (R_F). Here, $C_{dl}$was estimated by equation (1)[1-5]:

$$j_c = C_{dl} v \qquad (1)$$

where j_c (μA cm^{-2}) is charging current density and v (mV s^{-1}) represents the scan rate used in cyclic voltammetry.

The roughness factor for the electrocatalytic film on a conductive substrate plate can be calculated by equation (2).[3]

$$R_F = \frac{C_{dl}}{C_s} \qquad (2)$$

where C_s is the capacitance of ideally smooth oxide, 60 μF cm^{-2}.

The surface concentration of active sites (Γ_0) is reflected by the capacitance due to the phase change (C_p), which can be expressed as ($\Gamma_0 \propto C_p$). C_p is calculated through the CVs recorded with different scan rates (Fig. S11†). The Ni^{2+} oxidation is observed in the CVs. Fig. 9e demonstrates the linear relation between redox current density and scan rates. And the values for Γ_0 and TOF can be obtained by Eq. (3) and Eq. (4) respectively.[6]

$$\Gamma_0 = \frac{Slope \times 4RT}{n^2F^2A} \qquad (3)$$

where n is the electron transfer number, F is Faraday's constant (96485 C mol^{-1}), A is the surface area of the electrode (cm^2), R is the ideal gas constant (8.314 J·mol^{-1}·K^{-1}), and T is the absolute temperature (298.15 K)

$$TOF = \frac{J \times A}{4 \times F \times m} \qquad (4)$$

where J (A cm^{-2}) is the current density at a specific potential, 4 represents the

electrons consumed for evolving one mole of oxygen and m is the number of active sites.

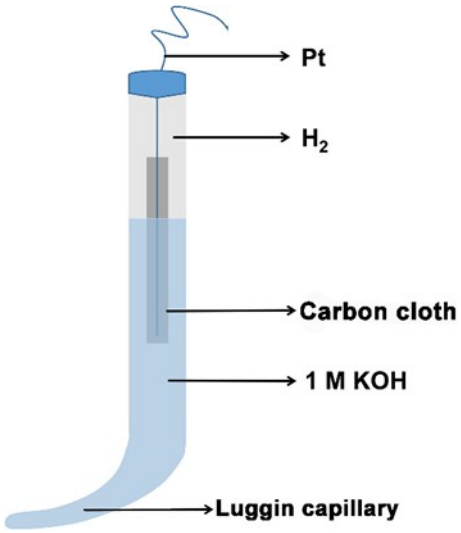

Fig. S1 illustration of the reversible hydrogen electrode.

The home-made reversible hydrogen electrode (RHE) was fabricated from a glass tube, with one end being a Luggin capillary structure and the other end sealed by glass fusion welding (Fig. S1).[7, 8] A Pt wire wrapped by a carbon cloth (Pt/C) is adopted to promise the formation of hydrogen gas diffusion layer. After filling the glass tube with 1 M KOH solution, constant-cell-voltage electrolysis at 10 V was conducted for 5 minutes in 1 M KOH electrolyte, with the above-mentioned Pt/C and a graphite rod as cathode and anode, respectively. Resultantly, the home-made RHE electrode filled with hydrogen in the sealed end (Fig. S1) was obtained.

Two ways are adopted to check the viability of the home-made RHE electrode. First, the open-circuit potential between two individually home-made RHE electrodes was tested, which is found to be close to zero, indicating that the potential difference between separately fabricated RHE electrodes is negligible. Besides, the open-circuit

potential between the home-made RHE electrode and a commercial Hg/HgO electrode is further tested, which is found to be ~0.924 V. Theoretically, the potential of the Hg/HgO electrode is 0.925 V vs. RHE electrode. [8-12] The measured value is very close to the theoretical value. The above results indicate that the home-made RHE reference electrode is applicable for the OER test.

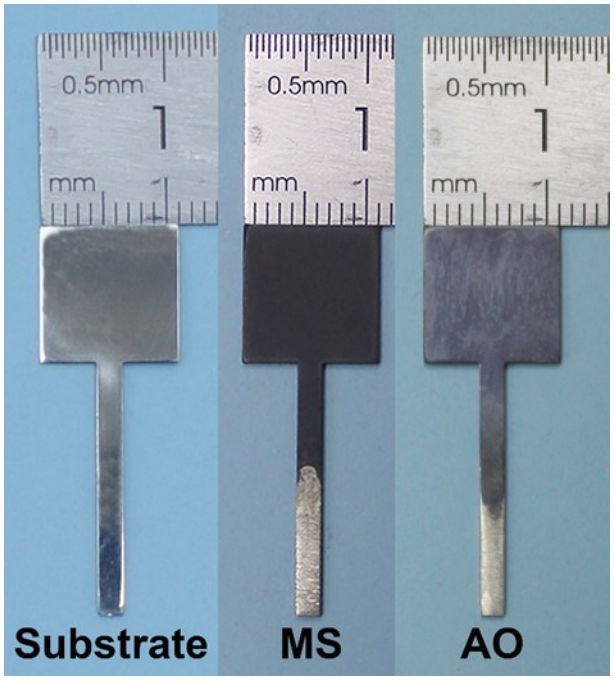

Fig. S2 Digital photos of the different samples.

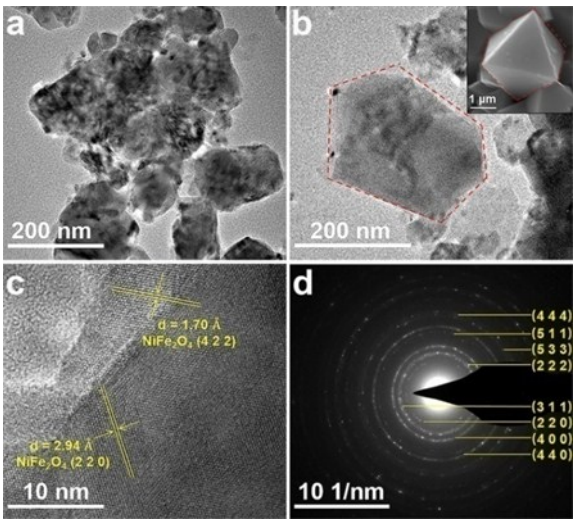

Fig. S3 TEM images (a and b), HRTEM image (c) and SAED pattern (d) of the powder scraped from the MS-derived film.

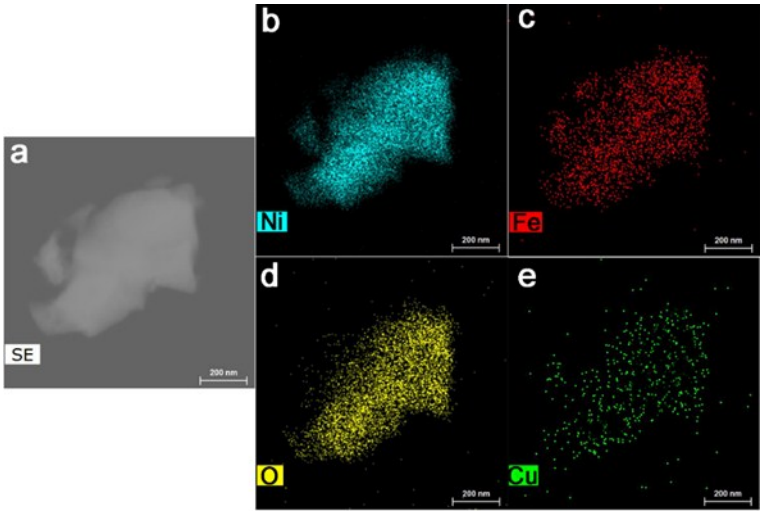

Fig. S4 TEM (a) and element distribution (b - e) of the particles scraped from the MS-derived film

Table S1. Contents of Ni, Fe and Cu in $NiFe_2O_4$ and the scraped particles from MS sample determined from ICP-OES

Sample	Ni (wt.%)	Fe (wt.%)	Cu (wt.%)
Scraped particles	46.5	33.0	4.0
Pure $NiFe_2O_4$	24.8	47.9	0

Table S2 Atomic ratio of elements for the films of MS and AO obtained from XPS results

	Fe/Ni (molar ratio)
MS-derived film	2.34
AO-derived film	1.22

Table S3 Fe $2p_{3/2}$ fitting parameters for $NiFe_2O_4$ suggested by Brisinger[13] and MS in this work

Fitting of Fe $2p_{3/2}$ for $NiFe_2O_4$ by Biesinger	**Fitting of Fe $2p_{3/2}$ for MS-derived film**
Peak1 position: 709.5 eV;	**Peak1 position**: 709.5 eV;
FWHM: 2.0 eV;	FWHM: 2.0 eV;
Area ratio: 34.1%	Area ratio: 20.8%
Peak2 position: 710.7 eV;	**Peak2 position**: 710.7 eV;
FWHM: 2.0 eV;	FWHM: 2.0 eV;
Area ratio: 33.2%	Area ratio: 41.9%
Peak3 position: 712.2 eV;	**Peak3 position**: 712.1 eV;
FWHM: 2.0 eV;	FWHM: 2.0 eV;
Area ratio: 22.3%	Area ratio: 26.6%
Peak4 position: 713.7 eV;	**Peak4 position**: 713.7 eV;
FWHM: 2.0 eV;	FWHM: 2.0 eV;
Area ratio: 10.4%	Area ratio: 10.7%

Notes: FWHM represents the peak width at half height; Area ratio is the percentage of total area.

Table S4 Ni $2p_{3/2}$ fitting parameters for $NiFe_2O_4$ suggested by Brisinger[13] and MS in this work

Fitting of Fe $2p_{3/2}$ for $NiFe_2O_4$ by Biesinger	**Fitting of Fe $2p_{3/2}$ for MS-derived film**
Peak1 position: 854.5 eV;	Peak1 position: 854.4 eV;
FWHM: 1.35 eV;	FWHM: 1.3 eV;
Area ratio: 17.3%	Area ratio: 17.5%
Peak2 position: 856.0 eV;	Peak2 position: 855.7 eV;
FWHM: 3.03 eV;	FWHM: 3.0 eV;
Area ratio: 38.2%	Area ratio: 41.1%
Peak3 position: 861.4 eV;	Peak3 position: 861.4 eV;
FWHM: 4.49 eV;	FWHM: 4.40 eV;
Area ratio: 38.5%	Area ratio: 36.7%
Peak4 position: 864.7 eV;	Peak4 position: 864.8 eV;
FWHM: 3.04 eV;	FWHM: 3.0 eV;
Area ratio: 2.8%	Area ratio: 1.63%
Peak5 position: 867.0 eV;	Peak5 position: 867.0 eV;
FWHM: 2.26 eV;	FWHM: 2.5 eV;
Area ratio: 3.2%	Area ratio: 3.07%

Notes: FWHM represents the peak width at half height; Area ratio is the percentage of total area.

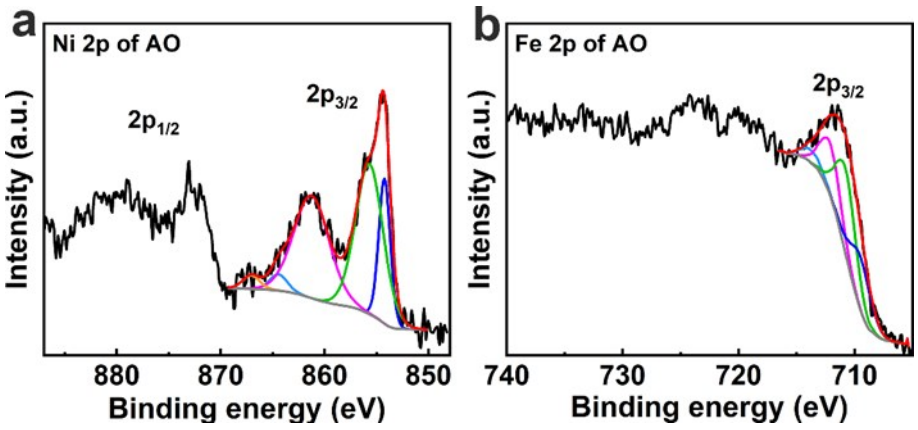

Fig. S5 Deconvolutions of the Ni 2p (a) and Fe 2p (b) spectrum of the AO sample.

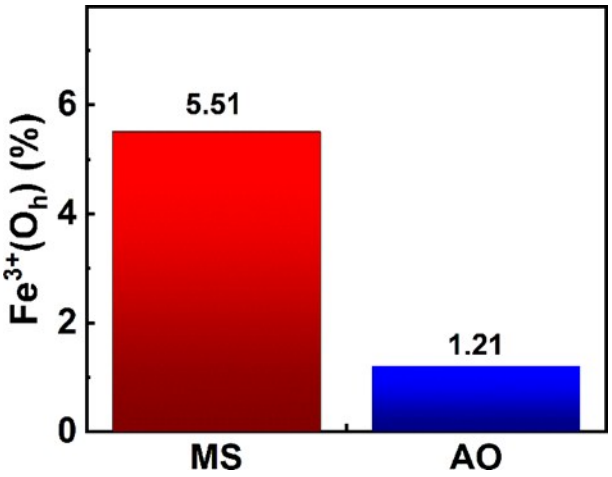

Fig. S6 the ratio of Fe^{3+} in octahedral site for the MS and AO films.

Fig. S6: According to the XPS survey spectra, the surface concentrations of Fe in **MS** and **AO** samples are 13.18% and 2.9%, respectively. The fitted peak located at 710.7 eV in the Fe 2p spectrum is attributed to $Fe^{3+}(O_h)$, which accounts for 41.9% in the MS-derived film (Table S3). Therefore, the surface concentrations of $Fe^{3+}(O_h)$ for **MS**-derived film is 5.51% (13.18%×41.9%=5.51%). Correspondingly, the value for AO-derived film is 1.21%.

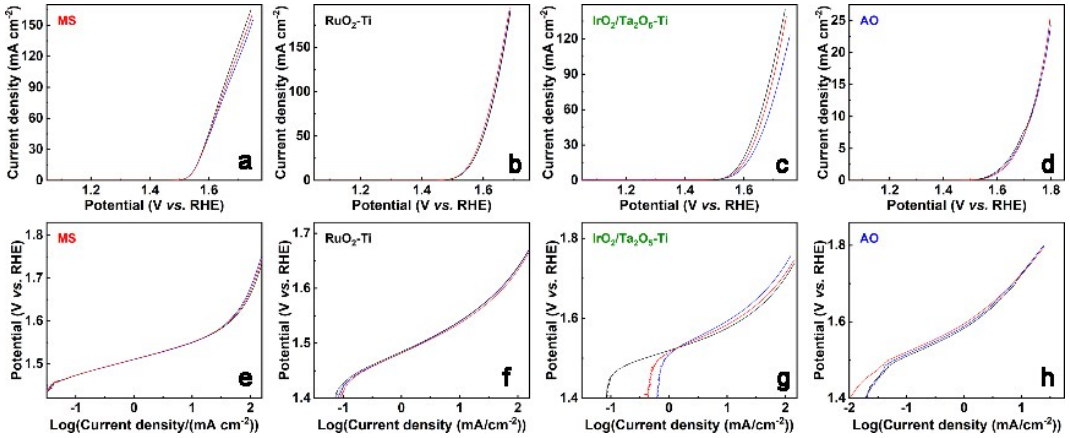

Fig. S7 Repeated LSV polarization curves (a - d) and corresponding Tafel plots (e - h) of the **MS**, RuO_2-Ti, IrO_2/Ta_2O_5-Ti and **AO** electrodes at 0.5 mV s^{-1} in 1 M KOH.

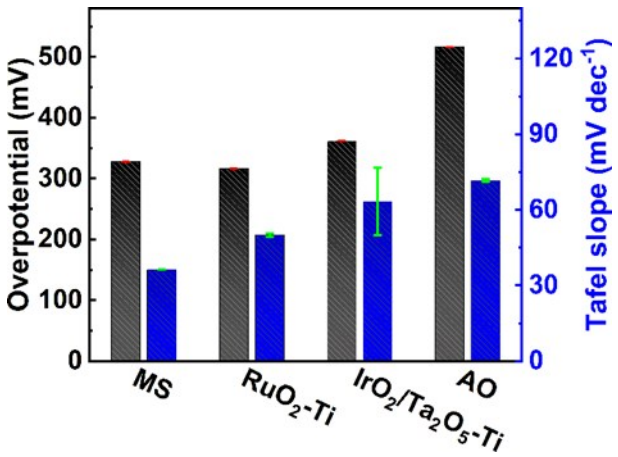

Fig. S8 the overpotential values at 10 mA cm^{-2} and Tafel slopes values of **MS**, RuO_2-Ti, IrO_2/Ta_2O_5-Ti and **AO** electrodes with standard deviations added.

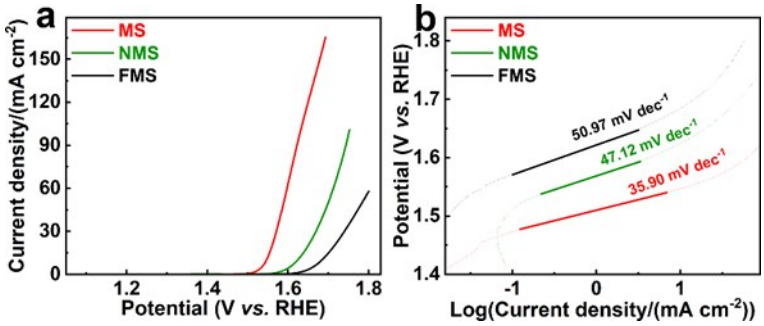

Fig. S9 (a) LSV polarization curves of the **MS**, **NMS** and **FMS** electrodes at 0.5 mV s^{-1} in 1 M KOH at 25 °C; (b) Corresponding Tafel plots of the samples.

Fig. S9: The polished nickel and iron plates (99.99% in purity) with the same size as **MS** electrode were treated by the same anodic oxidation in Na_2CO_3-K_2CO_3 molten salt. The obtained electrodes were noted as **NMS** and **FMS**. The OER activity of the electrodes was examined in 1 M KOH. Fig. S9 shows LSV curves and Tafel plots in 1 M KOH with a scan rate of 0.5 mV s^{-1}. Obviously, compared with the **NMS** and **FMS** sample, the MS presents a better OER activity in terms of overpotential and Tafel slope.

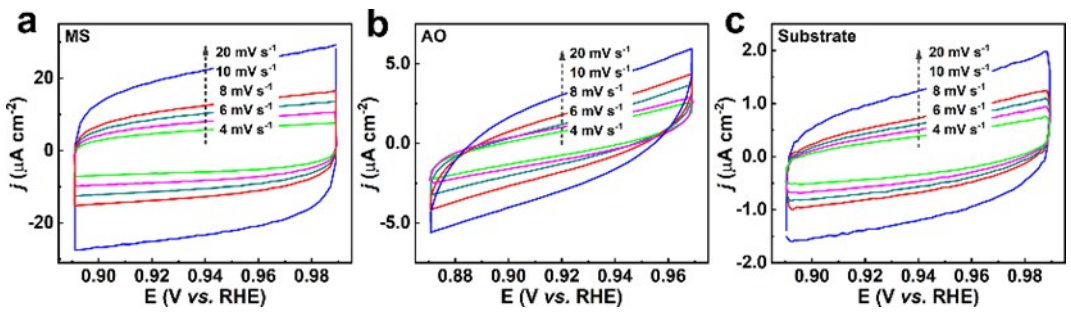

Fig. S10 CV curves of the (a) **MS** and (b) **AO** electrodes in the non-Faraday region at different scan rates in 1 M KOH electrolyte.

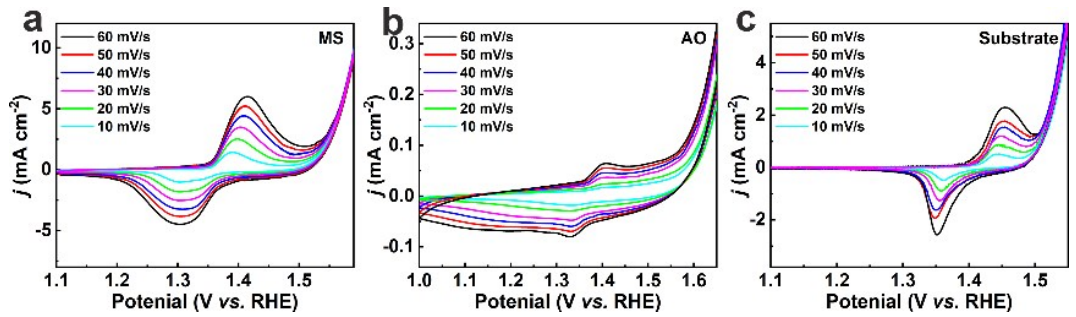

Fig. S11 CV curves of the (a) **MS** and (b) **AO** electrodes in the phase change region at different scan rates in 1 M KOH electrolyte.

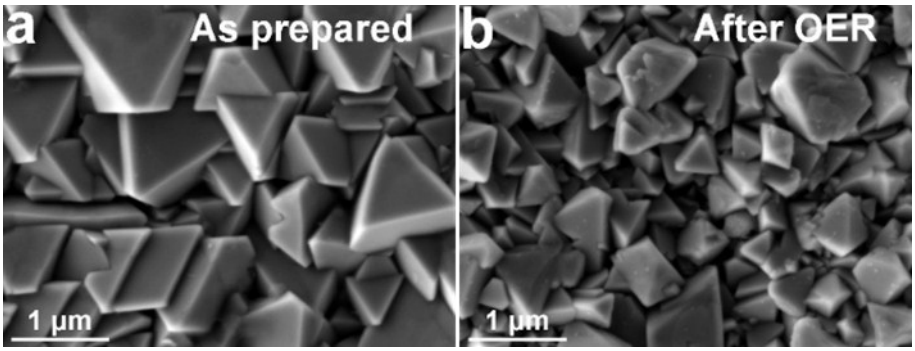

Fig. S12 Surface SEM imagines of the MS electrode before (a) and after (b) electrolysis at 50 mA cm^{-2} for 60 h in 1 M KOH.

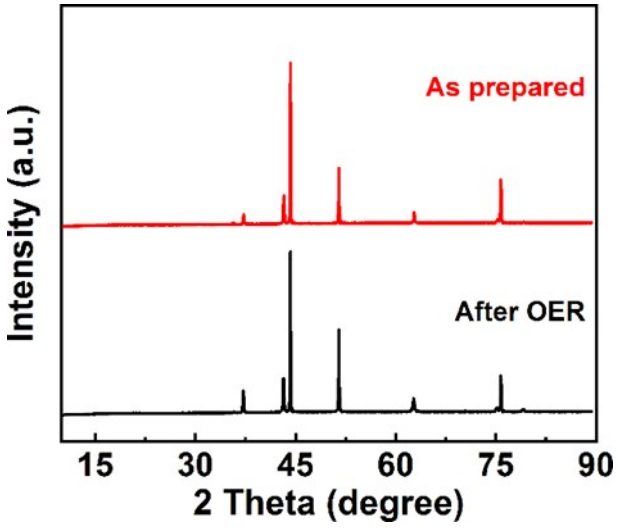

Fig. S13 XRD patterns of the MS electrode freshly prepared (in red) and after stability test (in dark grey).

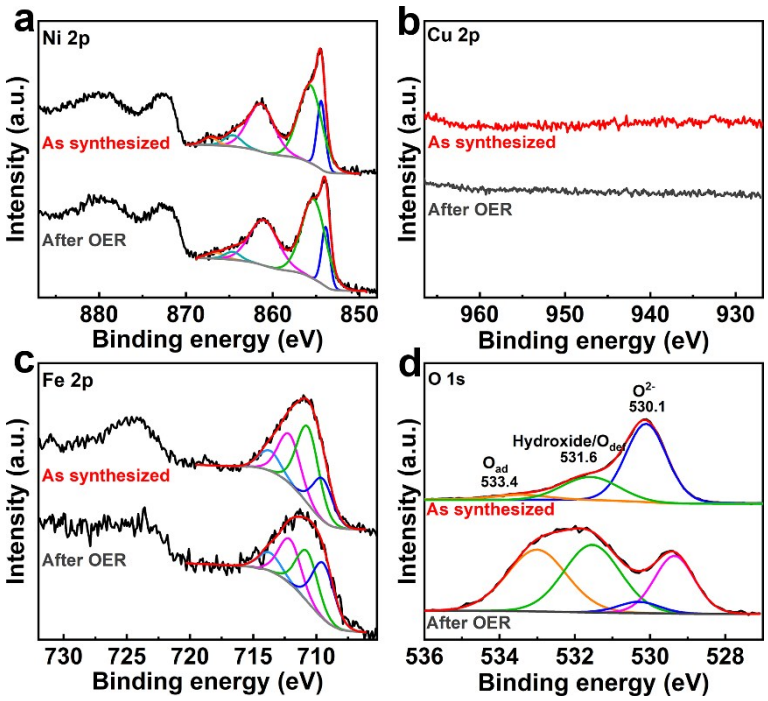

Fig. S14 XPS spectra for the surface of the MS-derived electrode before and after durability test: (a) Ni 2p; (b) Cu 2p; (c) Fe 2p and (d) O 1s.

Fig. S14: The XPS spectrum before and after stability tests are shown in Fig. S14. Negligible changes are observed for the Ni 2p, Fe 2p and Cu 2p spectra after 60 h electrolysis. For the O1s spectrum, intensity increase of peaks attributed to hydroxides and the surface adsorption oxygen are observed after stability tests, which is normal phenomenon for spinel oxides after OER catalysts. [14,15] The above results indicate that the MS-derived film shows a high structure stability for OER reaction.

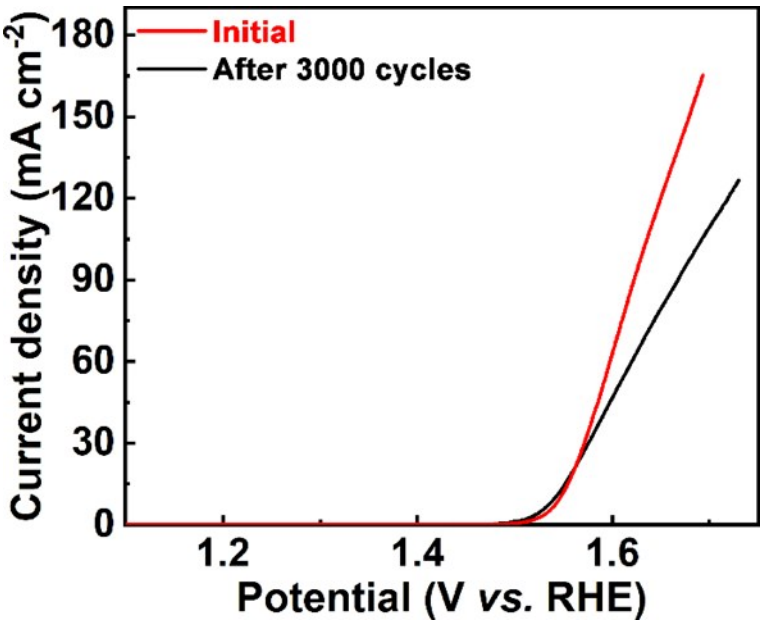

Fig. S15 LSV polarization curves of the MS before and after 3000 cycles of CVs in the potential range of 1.1 and 1.7 V vs. RHE at 50 mV s^{-1}

Table S5. **Ni-based film electrodes for OER in 1 M KOH solution**

Catalysts	Substrates	η* (mV)@ 10 mA cm^{-2}	Tafel slope (mV dec^{-1})	Ref.
$NiFe_2O_4$/NiO	Ni-11Fe-10Cu	326	36	This work
$Ni_{0.9}Fe_{0.1}O_x$	QCM	336	30	6
Ni(cyclam)-BTC	ITO	819	-	11
Hollow sphere NiO	GCE	370	156	12
Co-Ni-P	Ti sheet	340	67	13
NiCo LDH	Carbon paper	367	40	14
CoFeP HMSs	GCE	350	59	15
$CoFe_2O_4$	GCE	560	165	15
Spinel NiCo Oxide NRs	FTO	350	54	16
Spinel NiCo Oxide HNSs	FTO	340	51	16
Ni@NiO@C	GCE	380	55	17
CeO_2 - embedded NiO	GCE	382	118.7	18
NiO_x bulk	Ni	327	50	19
NiCd	Ti	382	59	20
NiFe	Ti	337	51	20
NiO-NF700	Ni foam	375	81	21
beta-$Ni(OH)_2$	GCE	340	38	22

* Overpotential

References

1. A. T. Swesi, J. Masud and M. Nath, *Energy Environ. Sci.*, 2016, **9**, 1771-1782.
2. G. Dong, M. Fang, J. Zhang, R. Wei, L. Shu, X. Liang, S. Yip, F. Wang, L. Guan, Z. Zheng and J. C. Ho, *J. Mater. Chem. A*, 2017, **5**, 11009-11015.
3. R. N. Singh, J. P. Pandey, N. K. Singh, B. Lal, P. Chartier and J.-F. Koenig, *Electrochim. Acta*, 1999, **45**, 1911–1919.
4. B. Bayatsarmadi, Y. Zheng, C. S. Casari, V. Russo and S. Z. Qiao, *Chem. Commun. (Camb)*, 2016, **52**, 11947-11950.
5. C. C. McCrory, S. Jung, J. C. Peters and T. F. Jaramillo, *J. Am. Chem. Soc.*, 2013, **135**, 16977-16987.
6. L. Trotochaud, J. K. Ranney, K. N. Williams and S. W. Boettcher, *J. Am. Chem. Soc.*, 2012, **134**, 17253-17261.
7. M. W. Louie and A. T. Bell, *J. Am. Chem. Soc.*, 2013, **135**, 12329-12337.
8 C. Xuan, K. Xia, W. Lei, W. Xia, W. Xiao, L. Chen, H. L. Xin and D. Wang, *Electrochim. Acta*, 2018, **291**, 64-72.
9 R.N. Singh, J.P. Pandey, N.K. Singh, B. Lal, P. Chartier and J.F. Koenig. *Electrochim. Acta*, 2000, **45**, 1911-1919.
10 Q. Zhao, Z. Yan, C. Chen and J. Chen. *Chem. Rev.*, 2017, **117**, 10121-10211.
11 X. Yu, M. Zhang, W. Yuan and G. Shi. *J. Mater. Chem. A*, 2015, **3**, 6921-6928.
12 M.W. Louie and A.T. Bell. *J. Am. Chem. Soc*., 2013, **135**, 12329-12337.
13 M.C. Biesinger, B.P. Payne, A.P. Grosvenor, L.W.M. Lau, A.R. Gerson and R.S.C. Smart. *Appl. Surf. Sci.*, 2011, **257**, 2717-2730.
14 J. He, Y. Sun, M. Wang, Z. Geng, X. Wu, L. Wang, H. Chen, K. Huang and S. Feng. *J. Alloy. Compd.*, 2018, **752**, 389-394.
15 F. Yan, C. Zhu, S. Wang, Y. Zhao, X. Zhang, C. Li and Y. Chen, *J. Mater. Chem. A*, 2016, **4**, 6048-6055.